ISSN 1028-3358, Doklady Physics, 2023, Vol. 68, No. 3, pp. 77–86. © Pleiades Publishing, Ltd., 2023.
Russian Text © The Author(s), 2023, published in Doklady Rossiiskoi Akademii Nauk. Fizika, Tekhnicheskie Nauki, 2023, Vol. 509, pp. 28–38.

MECHANICS

Experimental Study of the Nonmodal Perturbation Growth Mechanism in a Laminar Submerged Jet

D. A. Ashurov[a],*, V. V. Vedeneev[a],, L. R. Gareev[a],***, and O. O. Ivanov[a],******

Presented by Academician A.G. Kulikovskii May 31, 2022

Received May 31, 2022; revised May 31, 2022; accepted August 10, 2022

Abstract—It is known that, in wall-bounded flows, along with the growth of instability modes, an important role is played by the nonmodal (algebraic) mechanism of linear growth. In unbounded flows, including submerged jets, the nonmodal growth mechanism has been theoretically studied only in the last decade; this mechanism has not yet been identified in experiments. This paper describes experiments on excitation of the nonmodal "lift-up" growth mechanism. Special wavy structures (deflectors) are introduced into a laminar submerged jet of circular cross section, which excites a roller-like transverse motion. The data obtained make it possible to identify unambiguously the nonmodal lift-up growth of the introduced perturbations. The development of perturbations in the experiment qualitatively agrees with the theoretically calculated optimal perturbations. The specificities of the transition to turbulence caused by nonmodal growth are considered.

Keywords: submerged jet, optimal perturbations, nonmodal growth, laminar–turbulent transition

DOI: 10.1134/S1028335823020015

1. INTRODUCTION

Submerged jets are widely used in science and technology. In studying the physical processes accompanying combustion, mixing, chemical processes, spraying, acoustic radiation, etc., the stability of jets and the transition to turbulence play an important role.

Laminar submerged jets are often considered practically unstable, since the critical Reynolds number in them does not exceed 40. In practice, such jets have a region with a laminar structure, but it is usually relatively small (on the order of 1–2 diameters of the exit section). For this reason, it is extremely difficult to study the mechanisms of perturbation growth in the laminar section, leading to a laminar–turbulent transition, on "ordinary" jets.

The setup described in [1, 2] makes it possible to create submerged air jets with a much larger laminar section, up to $6D$, where D is the jet diameter. It was used to study experimentally the development of the jet's eigenmodes. The wavelengths of growing perturbations, the perturbation amplification curves, and the radial perturbation distributions found in the experiment qualitatively and quantitatively agree with the numerical values obtained within the linear theory [3, 4]. Thus, it was shown that the small sinusoidal perturbations introduced in the experiment develop in accordance with the linear stability theory.

The aim of this work is to study experimentally the nonmodal development of perturbations in a submerged jet. It is well known [5] that, in addition to the modal mechanism of linear growth in boundary layers, there are two mechanisms of nonmodal linear growth: the Orr mechanism and the "lift-up" mechanism. The first one is a purely two-dimensional process and leads to relatively weak growth, while the second gives a much stronger growth of three-dimensional perturbations and is responsible for the bypass transition in near-wall flows [6, 7]. In submerged jets, the existence of these two growth mechanisms has also been shown theoretically [8–10]. However, they have not yet been detected experimentally.

In this study, we consider a laminar jet air flow formed with a device of a special type, described in detail in [1, 2]. The initial jet diameter is $D = 120$ mm, and the outflow regime corresponds to a velocity on the axis $U_{max} = 1.5$ m/s, an average velocity $U_{av} = 0.66$ m/s, and the Reynolds number, based on the average velocity and diameter, Re = 5400. The jet velocity profile is shown in Fig. 1. Downstream evolution of the undisturbed profile at distances $z/D < 5$,

[a] *Institute of Mechanics, Moscow State University, Moscow, 119991 Russia*

**e-mail: ashurovda@my.msu.ru*

***e-mail: vasily@vedeneev.ru*

****e-mail: gareev.lr@yandex.ru*

*****e-mail: ivanov@imec.msu.ru*

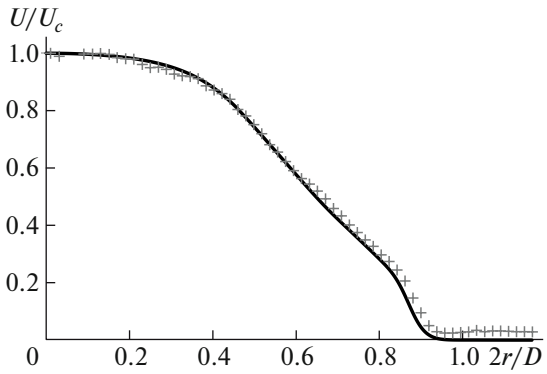

Fig. 1. Velocity profile of the flow under study: (crosses) experimental values obtained with a hot-wire anemometer and (solid line) the approximated profile.

considered in the experiments, is weak and is not taken into account in theoretical calculations. The experimental profile was spline-approximated for theoretical study.

2. THEORETICAL ANALYSIS OF SPATIAL NONMODAL INSTABILITY

The study of the nonmodal instability of the flow begins with the search for eigenmodes of the velocity profile of the jet formed. The velocity components and pressure with small perturbations are substituted into the dimensionless equations of motion of a viscous incompressible fluid, and the resulting equations are linearized.

Perturbations are considered in the form of eigenmodes:

$$\begin{bmatrix} u \\ v \\ w \\ p \end{bmatrix}(r,\theta,z,t) = e^{i(\alpha z + n\theta - \omega t)} \begin{bmatrix} iF \\ G \\ H \\ P \end{bmatrix}(r). \qquad (1)$$

For a given real frequency ω and an integer azimuthal wavenumber n, the eigenvalue (α) problem is solved using the spectral method [11]. Thus, for the velocity profile under consideration, we find N eigenvalues α_j, $j = 1,\ldots,N$, in a viscous linear formulation.

An arbitrary perturbation with given ω and n can be represented as

$$\mathbf{q}(r,\theta,z,t) = \sum_{j=1}^{N} \gamma_j \mathbf{q}_j(r) e^{i(\alpha_j z + n\theta - \omega t)}, \qquad (2)$$

where $\mathbf{q} = (iF, G, H, P)$ is the system state vector and α_j and $\mathbf{q}_j$ are the jth eigenvalue and the corresponding eigenvector. In this expansion, only downstream eigenmodes are taken into account. The norm of the functional characterizing the perturbation is understood as kinetic energy in the form

$$E(z) = \frac{1}{4\pi T} \int_0^{\infty} \int_0^{T} \int_0^{2\pi} ((\mathrm{Re}u)^2 + (\mathrm{Re}v)^2 + (\mathrm{Re}w)^2) r d\theta dt dr, \qquad (3)$$

$$T = \frac{2\pi}{\omega}.$$

For stationary perturbations, we consider the limit of this expression at $\omega \to 0$. The kinetic energy of the perturbation is a quadratic function of the coefficients of the eigenmode expansion of the perturbation. Thus, the problem of optimal perturbations, i.e., perturbations growing faster than others at a given longitudinal coordinate z, reduces to a constrained optimization problem:

$$\gamma^{\dagger} \mathbf{E}(z) \gamma \to \max, \quad \text{subject to the constraint} \quad \gamma^{\dagger} \mathbf{E}(0) \gamma = 1, \qquad (4)$$

where γ is the column vector of the spectral expansion coefficients, $E(z)$ is the matrix generated by functional (3), and † denotes Hermitian conjugation.

It was shown in [8] that, for several types of jet flows, the maximum nonmodal growth is demonstrated by stationary perturbations (i.e., perturbations with $\omega \to 0$). For the profile under consideration, its stationary perturbations also turned out to be optimal. The dependences of the relative kinetic energy of the optimal perturbations on the distance downstream were found (Fig. 2a) for various azimuthal numbers $n = 1,2,3,4,5$. Each curve in Fig. 2 comprises the envelope of the family of curves for the relative kinetic energy of all possible stationary perturbations for a given n:

$$G(z) = \max \frac{E(z)}{E(0)},$$

where the maximum is taken over all perturbations with given n. It can be seen that, at small z, perturbations with different n grow at close rates, but, with increasing z, it is clear that the maximum kinetic energy is specific for the perturbation with $n = 1$; with increasing n, the kinetic energy of the optimal perturbations decreases.

Due to the axial symmetry of the unperturbed profile, for each $n \neq 0$, there is an optimal perturbation twisted counterclockwise and a similar perturbation twisted in the opposite direction, for $-n$. In order to obtain the optimal solution without twisting, we will carry out the following transformations:

$$\tilde{\mathbf{q}}^n(r,\theta,z) = \frac{\mathbf{q}^n(r,\theta,z) e^{in\theta} + \mathbf{q}^{-n}(r,\theta,z) e^{-in\theta}}{2}, \qquad (5)$$

where $\mathbf{q}^n$ is the optimal perturbation for a given n. Three optimal perturbations—two twisted in opposite

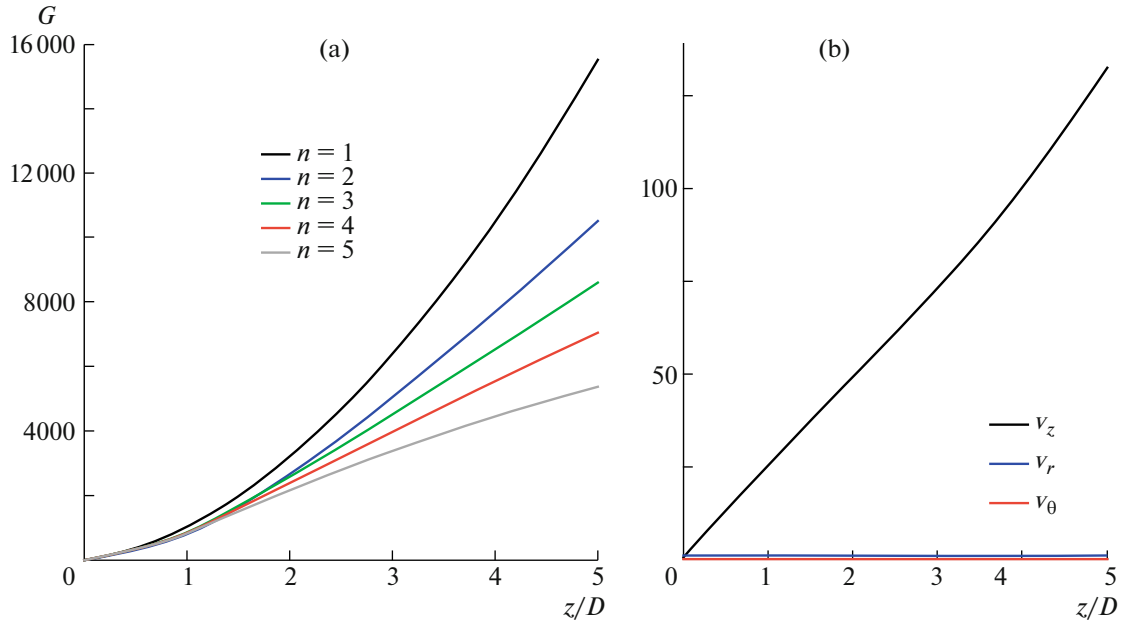

Fig. 2. (a) Energy growth of stationary optimal perturbations downstream for various azimuth numbers n. (b) Optimal perturbation velocity components for $n = 2$.

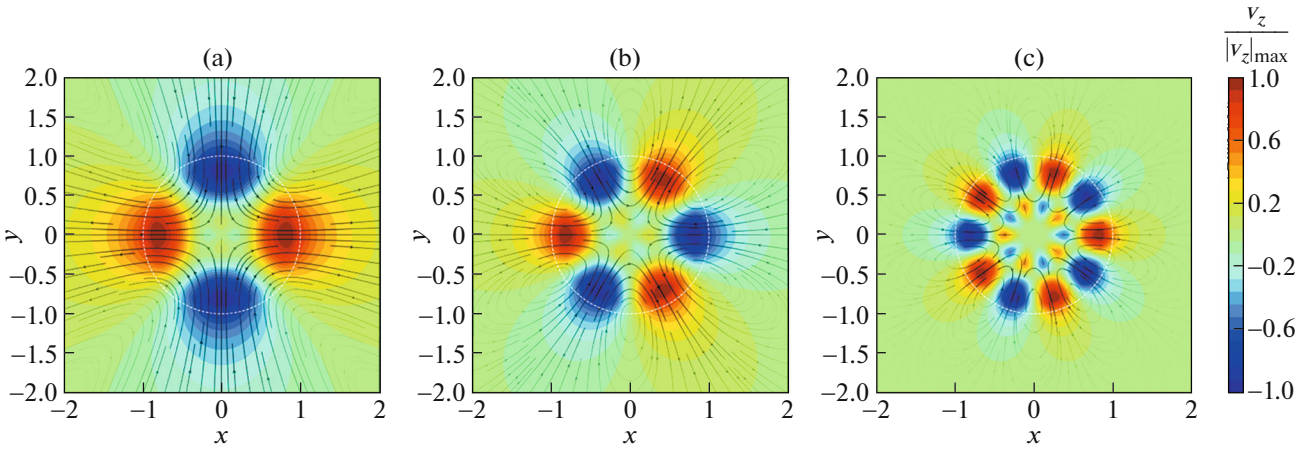

Fig. 3. Distribution of the longitudinal component of the optimal perturbation velocity and the streamlines in the jet cross section for (a) $n = 2$, (b) $n = 3$, and (c) $n = 5$ at the z coordinate at which the global energy maximum is reached.

directions and one without twisting—are equivalent and have the same kinetic energy growth rate.

Visualizations of the obtained optimal perturbations without twisting, on which the maximum $G(z)$ is reached, are shown in Figs. 3, where the perturbation of the longitudinal velocity is shown in color, the streamlines are drawn for transverse velocities (a larger value of the transverse velocity corresponds to thicker sections of the streamlines), and the white circle is the unperturbed jet boundary. As can be seen, in the case of $n \geq 1$, the optimal perturbation comprises several vortex structures (the number of which is $2n$), which form zones of jet acceleration and deceleration due to the replacement of fast layers by slow ones, and vice versa. Such a structure resembles the lift-up mechanism in the boundary layer.

Figure 2b shows $n = 2$ as an example, the plots of the root-mean-square values of the pulsations of the longitudinal and transverse velocities of the globally optimal perturbation (i.e., the perturbation on which $\max_z G(z)$ at $\omega \to 0$ is reached) as functions of the longitudinal coordinate z at $2r/D = 0.75$ and $\theta = 0$. It can be seen that the longitudinal velocity increases

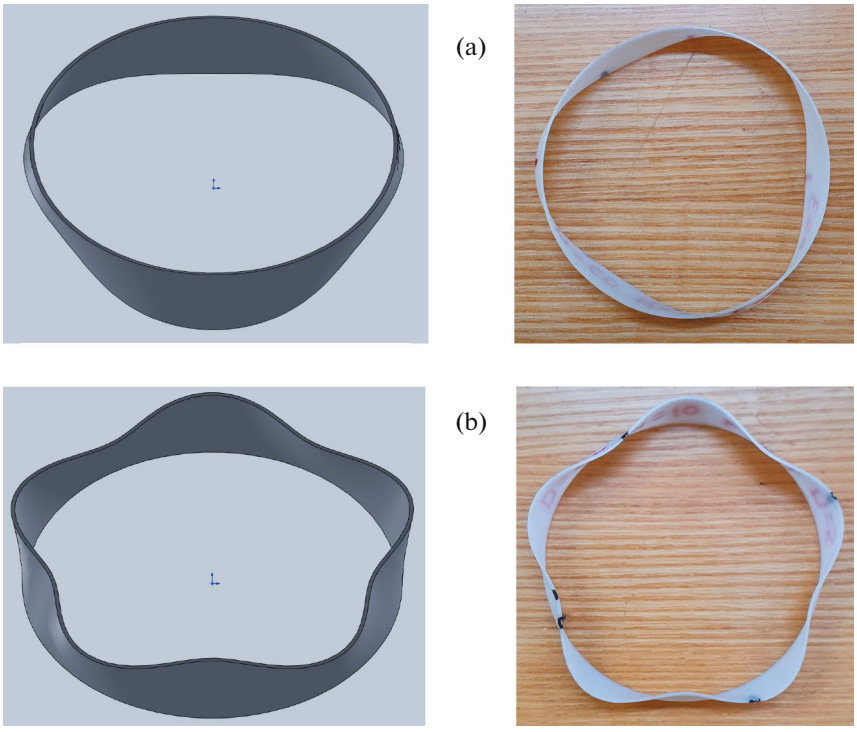

Fig. 4. (Left) 3D model and (right) fabricated deflector with azimuth numbers (a) $n = 3$ and (b) $n = 5$, with parameters $\varepsilon = 0.1$, $h = 10$ mm, and $d_0 = 60$ mm.

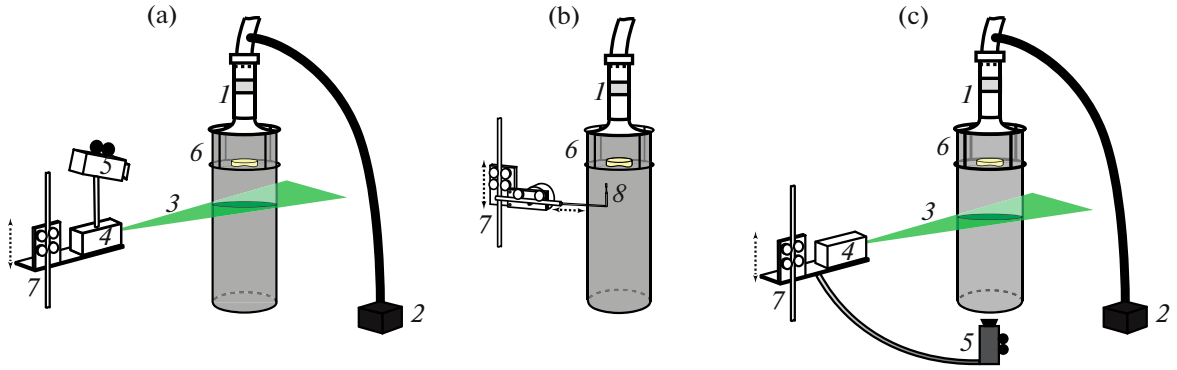

Fig. 5. Schematics of the (a) flow visualization in the transverse plane, (b) measurements with a hot-wire anemometer, and (c) PIV measurements in the transverse plane: (*1*) diffuser, (*2*) glycerin aerosol generator, (*3*) laser knife, (*4*) laser, (*5*) video camera, (*6*) fixture with deflector, (*7*) moving device, and (*8*) hot-wire anemometer sensor.

approximately linearly, while the transverse velocities practically do not change downstream. This feature—the development of perturbations of longitudinal velocity with the preservation of longitudinal vortices—is characteristic of the nonmodal lift-up perturbation growth mechanism.

As can be seen, for the profile considered, the optimal perturbations have a complex three-dimensional structure and, therefore, are difficult to realize experimentally. In the experiments described below, with the help of special deflectors, an attempt is made to create perturbations that are qualitatively close to that theoretically optimal.

3. EXPERIMENTAL STUDIES

3.1. Method for Jet Perturbation

The theory shows that stationary perturbations are "optimal" in comparison with nonstationary ones in the sense that their relative kinetic energy grows faster. In this regard, perturbations were introduced into the jet using motionless thin wavy structures: deflectors

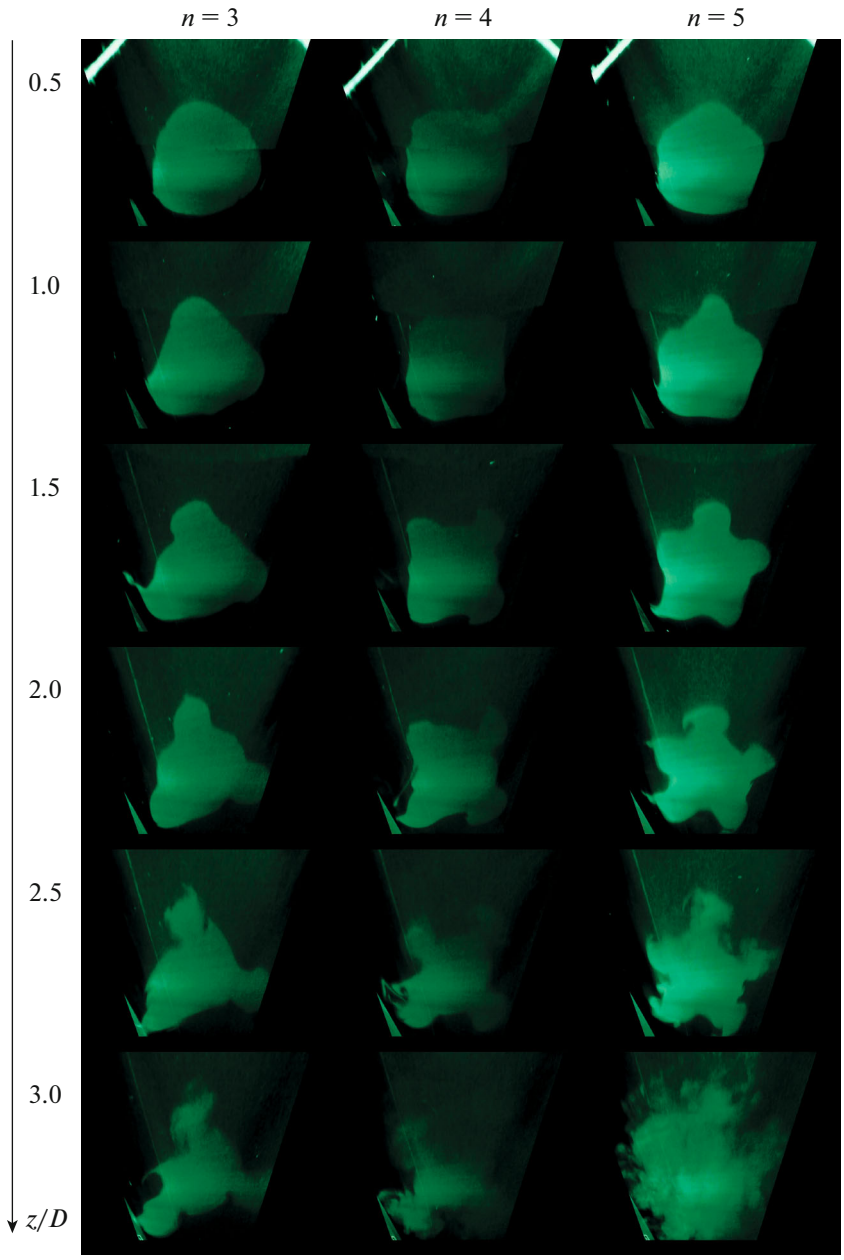

Fig. 6. Evolution of stationary perturbations introduced by deflectors with azimuthal numbers $n = 3,4,5$ and $\varepsilon = 0.1$ in photographs of the cross section.

(Fig. 4). The upper edge of the deflectors had the form of a circle of radius $r_0 = d_0/2$, and the lower edge, the form of a perturbed circle with a given azimuth number n and radius $r = r_0(1 + \varepsilon\sin(n\theta))$, where ε specifies the dimensionless amplitude of deviation from the circle. The height of the deflector between the upper and lower edges is h. A smooth transition is made between the edges (points of the upper and lower edges with the same azimuthal coordinate θ were connected by straight line segments). The models were designed in the CAD program and then 3D printed from PLA plastic (polylactide). The results presented below were obtained with deflectors with $h = 10$ mm, $d_0 = D/2 = 60$ mm, and $\varepsilon = 0.05$ and 0.1.

To introduce a perturbation into the jet, the deflectors were placed coaxially in the jet at a distance of $z = 20$ mm, i.e., at $z/D = 1/6$ (hereinafter, the distance z is measured from the exit section of the diffuser downwards), with the unperturbed edge upwards (the entry section of the deflector is a circle). The lower edge of the deflectors is located on thin stretched lines (line diameter 0.05 mm).

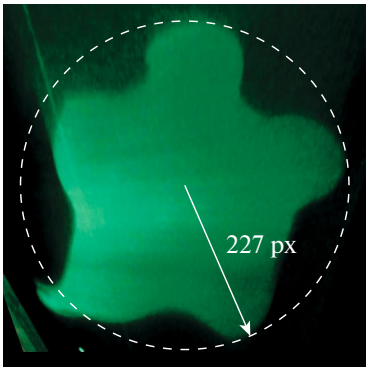

Fig. 7. An example of finding the petal radius from the perturbed jet cross section. A deflector with $n = 5$ and $\varepsilon = 0.1$ is placed in the jet. The downstream distance is $z = 1.5D$.

3.2. Visualization of Perturbation Development

The visualization of the flow (Fig. 5a) was carried out by the laser knife method. Fine glycerol particles (particle diameter of 1–3 μm) were added to the streamline before the forming device, and a continuous green laser with a wavelength of 532 nm, equipped with a cylindrical lens to create a cut plane, illuminated the jet cross section. The video camera was out of the flow and was mounted on a single-coordinate moving device together with the laser and, accordingly, moved synchronously with the illuminated cross section of the jet to ensure the same frame scale for each shooting height. All frames of the cross section at distances $z/D = 0.5...3.5$ were obtained at an angle to the jet axis; therefore, a linear transformation of the frame plane was subsequently carried out to eliminate its distortion.

Perturbations from deflectors at small distances from the diffuser practically do not deform the cross section, but, with the development of a stationary perturbation downstream, the cross section changes, acquiring the shape of the exit part of the deflectors (Fig. 6). There is an increase in the "petals," their elongation in the radial direction from the jet axis, and the formation of a "neck": a narrow part of the jet section connecting the petal with the jet core. Soon after the neck formation, a strong increase in the nonstationarity and destruction of the jet at distances $z/D \sim 3$ is observed.

From the cross sections of the jet with perturbations introduced into it from the deflectors with $n = 3, 4, 5$, we obtained the dependences of the petal radius on the downstream distance z, as shown in Fig. 7. Based on the experimental dependences shown in Figs. 8, it can be seen that the petals elongate linearly; therefore, the perturbation velocity in the radial direction is constant. For stationary perturbations, which are optimal for the jet considered, the downstream radial velocity also preserves its value (see Section 2).

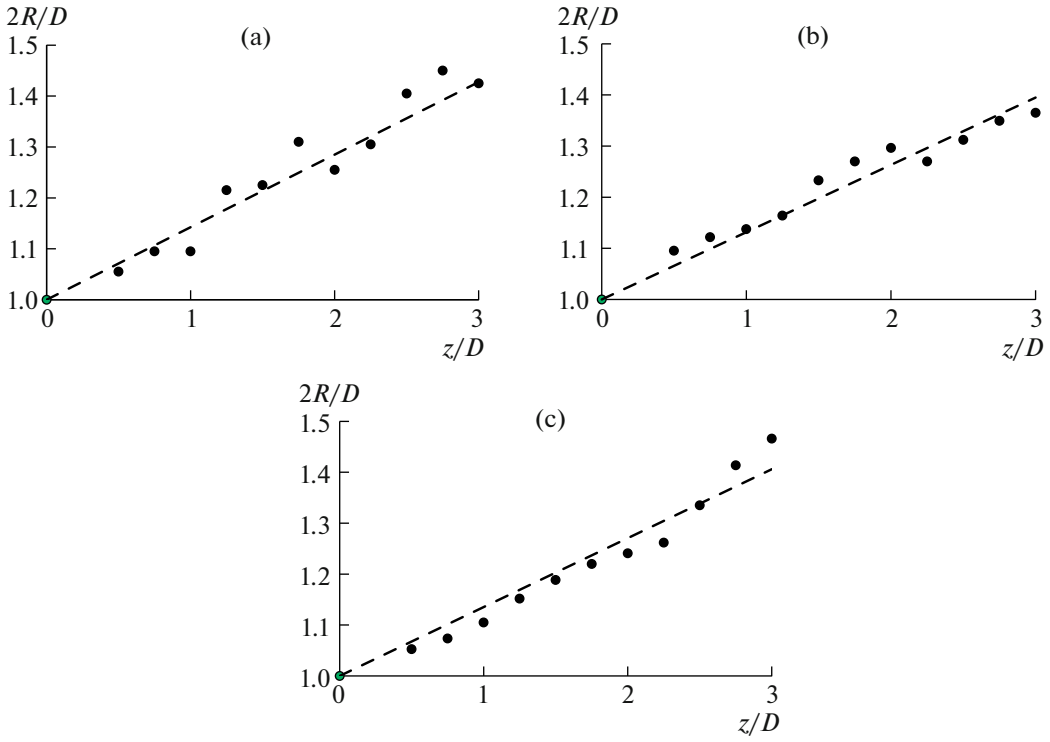

Fig. 8. Petal length vs. distance z downstream for (a) $n = 3$, (b) $n = 4$, and (c) $n = 5$.

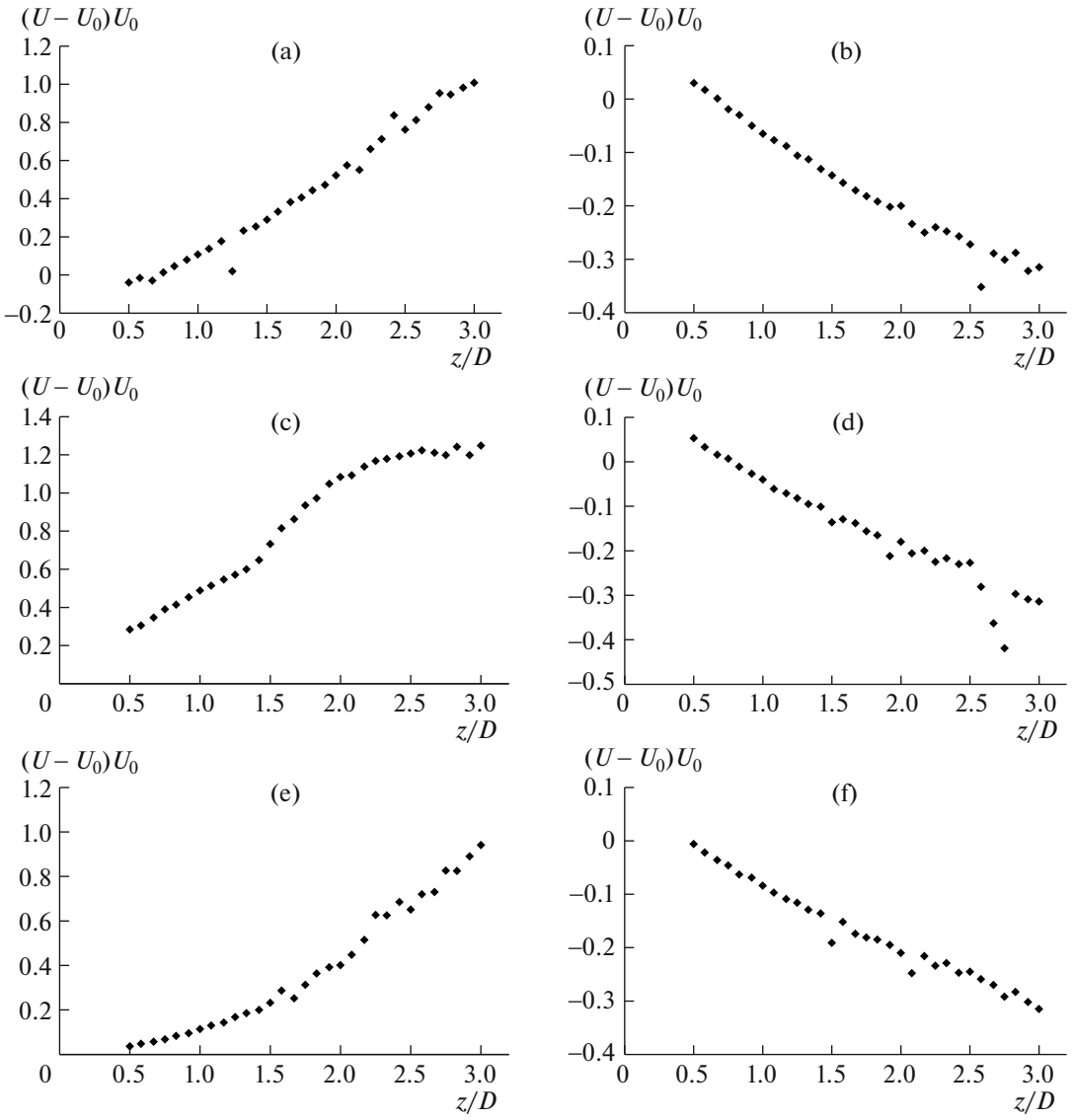

Fig. 9. Longitudinal flow velocity vs. distance z downstream: (a) $n = 3$ and $2r/D = 0.78$; (b) $n = 3$ and $2r/D = 0.58$, (c) $n = 4$ and $2r/D = 0.73$, (d) $n = 4$ and $2r/D = 0.58$, (e) $n = 5$ and $2r/D = 0.78$, and (f) $n = 5$ and $2r/D = 0.58$, at points (left) in petals and (right) in "troughs".

3.3. Measurements of the Development of the Longitudinal Velocity Component

To make sure that the development of perturbations introduced by the deflectors qualitatively corresponds to the development of optimal perturbations for the jet profile considered, it is necessary to understand the character of the change in the longitudinal downstream flow velocity. For this purpose, a series of experiments was carried out to determine the average velocity with a hot-wire anemometer in a narrow region outside the flow core with deflectors $n = 3, 4, 5$. The measurement was made using a DISA CTA BRIDGE 56C17 hot-wire anemometer. The hot-wire anemometer sensor is located at the end of an L-shaped holder (Fig. 5b), the movement of which in the transverse and longitudinal directions of the jet flow is controlled from a PC using a specially developed program in the LabView environment.

The measurement results are shown in Fig. 9 for deflectors with $\varepsilon = 0.05$ and points with fixed radial and azimuthal coordinates (so that the dependences obtained are not affected by the trace from the deflector). The graphs show the dependences of the relative amplitude of stationary perturbations on z/D at the points corresponding to the petals of the jet cross section on the graphs on the left and at the points corre-

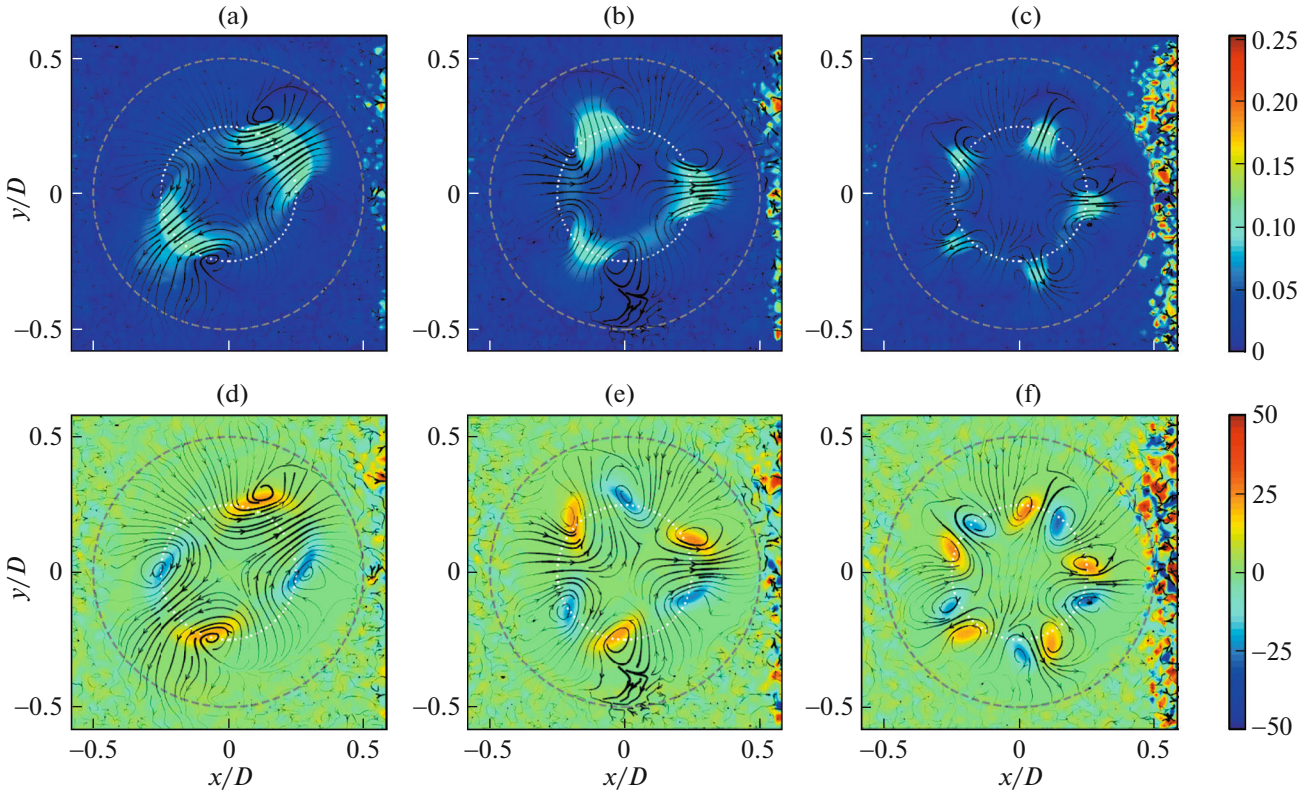

Fig. 10. (a–c) Transverse velocity (m/s) and (d–f) vorticity (1/s) with plotted streamlines for the perturbation for $n = 2$ (a, d), 3 (b, e), 5 (c, f) at $z/D = 1$.

sponding to the troughs on the graphs on the right. According to these dependences, it can be said that, in the places of contraction and expansion of the flow, the longitudinal velocity changes according to a nearly linear law.

The nearly linear increase in the longitudinal velocity is in accordance with the character of the growth of theoretical optimal perturbations, in which the longitudinal velocity also increases linearly (see Section 2).

3.4. PIV Measurements of Transverse Velocity

The method for seeding the flow for PIV measurements was the same as for flow visualization. The flow was illuminated with a Beamtech Vlite-Hi-100 high-frequency pulsed NG:Yag laser mounted on a coordinate-moving device; a rod with an Allied Vision Bonito CL-400B high-speed PIV camera was attached to it. When measuring the cross section, the camera was placed directly into the jet at a distance of 720 mm below the measured cross section (Fig. 5c). Double-frame shooting was carried out mainly with a frequency of 20 Hz. The average velocity field was found by averaging 3000 instantaneous velocity fields. Each experiment for a separate deflector consisted of putting it into the flow and measuring the average transverse velocity.

To analyze the features of the perturbation, below we give the averaged perturbation fields, i.e., the perturbation flow minus the main flow, on which the streamlines plotted from the transverse perturbation velocity are superimposed. Figure 10 shows the flow patterns behind deflectors with $n = 2$, 3, 5 and $\varepsilon = 0.05$, taken at $z/D = 1$, with plotted streamlines. The upper figure shows the pattern of the transverse velocity (shading corresponds to the magnitude of the velocity), and the lower figure shows the pattern of the longitudinal vorticity component ω_z. The thicker parts of the streamlines correspond to a greater magnitude of the transverse velocity. The large gray dotted ring has a diameter of 120 mm and corresponds to the boundaries of the undisturbed jet, and the small dotted ring with a diameter of 60 mm corresponds to the location of the deflector.

The exit section of the deflector at $n = 2$ is characterized by two minima and two maxima, which is also reflected in the perturbation patterns (Figs. 10a, 10d). In the direction of antinodes-maxima, corresponding to the maximum radius of the deflector, there is a distinct flow from the axis to the periphery and, for antinodes-minima, towards the axis. Between these

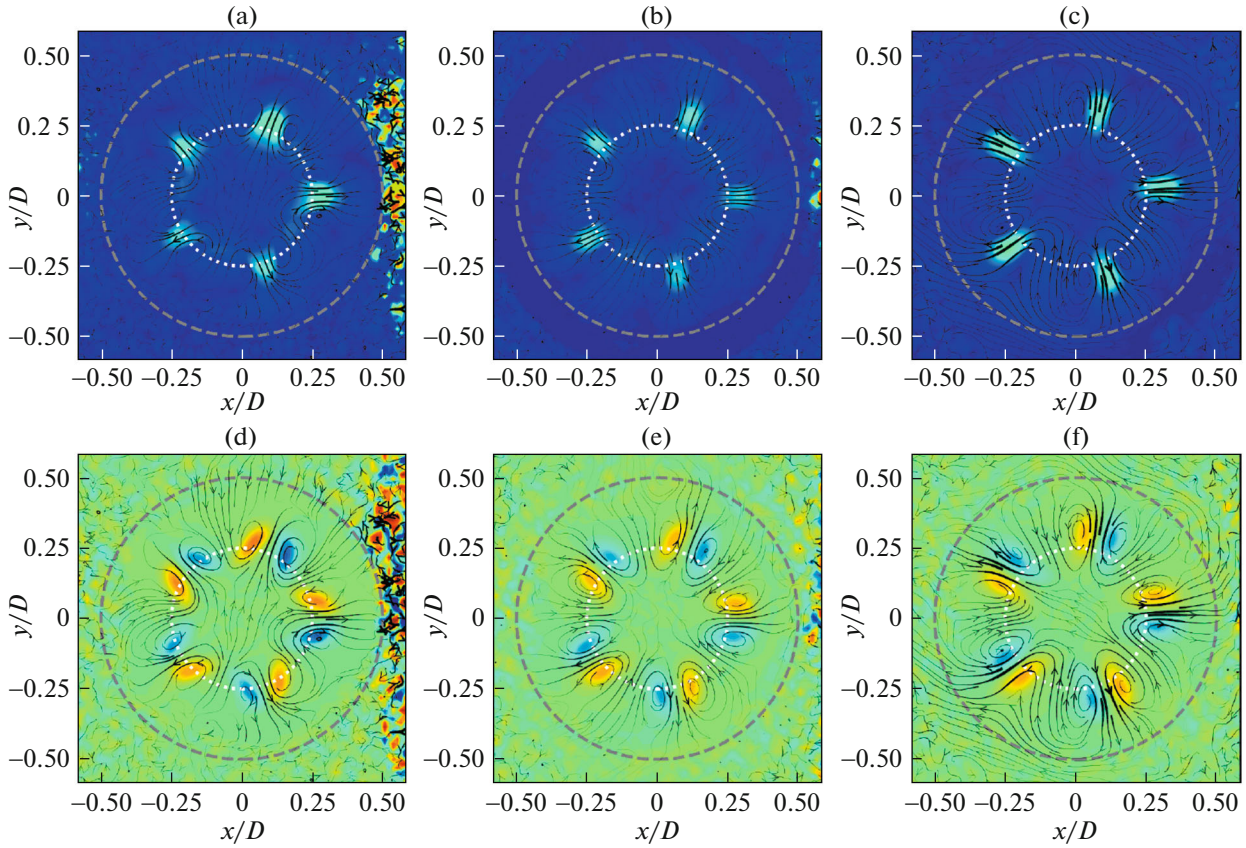

Fig. 11. Perturbation evolution downstream for $n = 5$: (top) velocity magnitude and (bottom) vorticity; (a, d) $z/D = 1$; (b, e) $z/D = 1.5$; and (c, f) $z/D = 2$.

regions, eddies are observed, indicated by the vorticity maxima and minima in Fig. 10d.

At $n = 3$, the flow pattern (Figs. 10b, 10e) is similar: each of the three perturbation petals produces two eddies fringing them, which capture the region of low longitudinal velocity located on the periphery and transfer it towards the jet axis, while the region of high longitudinal velocity located near the axis is transferred to the periphery.

Figures 10c and 10f show the flow patterns for $n = 5$. With an increase in n, there is a tendency to change the angle of inclination of the vortex regions, and the vortex zones are more and more aligned in the radial directions passing through the center of the petal.

Let us trace the change in the downstream flow pattern for $n = 5$ (in other cases, the pattern is qualitatively similar). Figure 11 shows the perturbation patterns at $z/D = 1, 1.5, 2$. The perturbation undergoes a certain deformation, but the flow structure does not change. The increased-velocity zones gradually shift to the periphery, to the zone of lower velocities of the main stream, which corresponds to the elongation of the petals observed in the flow visualization (Subsection 3.2). The values of the transverse velocity practically do not change downstream. The eddies separating the petals gradually weaken, and the maximum vorticity magnitudes decrease.

4. CONCLUSIONS

In this study, for the first time, a nonmodal mechanism of the growth of stationary perturbations in a jet flow, an analogue of the lift-up growth mechanism in the boundary layer, has been detected experimentally. The following characteristic features of the lift-up mechanism have been confirmed:

(a) The lateral velocity remains approximately constant downstream.

(b) The longitudinal velocity increases downstream approximately linearly.

(c) The transverse motion has the form of roller-like movements, transferring the outer fluid layers inwards and the inner layers outwards. This motion causes a local increase in the perturbation of the longitudinal velocity, which is analogous to the streaky structures in the boundary layers.

The jet development has been traced to the transition to turbulence, which is preceded by the separation

of the jet petals from the main flow and the formation of necks, followed by a rapid increase in the unsteadiness and turbulization of the jet.

Thus, the suppression of the modal growth of Kelvin–Helmholtz waves and the excitation of the nonmodal lift-up growth mechanism demonstrated in this work leads to a bypass scenario of transition to turbulence, which has not been previously observed in jet flows. Further study of this transition scenario, including the transition caused by a combination of modal and nonmodal mechanisms of linear perturbation growth, can find application in various technical devices for intensifying mixing and heat transfer.

FUNDING

This work was supported by the Russian Science Foundation, grant no. 20-19-00404.

CONFLICT OF INTEREST

The authors of this work declare that they have no conflicts of interest.

REFERENCES

1. Yu. S. Zaiko, A. I. Reshmin, S. Kh. Teplovodskii, and A. D. Chicherina, Fluid Dyn. **53**, 95 (2018).
2. J. Zayko, S. Teplovodskii, A. Chicherina, V. Vedeneev, and A. Reshmin, Phys. Fluids **30**, 043603 (2018).
3. Yu. S. Zayko, L. R. Gareev, A. D. Chicherina, V. V. Trifonov, V. V. Vedeneev, and A. I. Reshmin, Phys. Dokl. **66**, 106 (2021).
4. L. R. Gareev, J. S. Zayko, A. D. Chicherina, V. V. Trifonov, A. I. Reshmin, and V. V. Vedeneev, J. Fluid Mech. **934**, A3 (2022).
5. B. F. Farrell and P. J. Ioannou, Phys. Fluids A **5**, 1390 (1993).
6. P. Andersson, M. Berggren, and D. S. Henningson, Phys. Fluids **11**, 134 (1999).
7. M. Matsubara and P. H. Alfredsson, J. Fluid Mech. **430**, 149 (2001).
8. S. A. Boronin, J. J. Healey, and S. S. Sazhin, J. Fluid Mech. **716**, 96 (2013).
9. J. I. Jimenez-Gonzalez, P. Brancher, and C. Martinez-Bazan, Phys. Fluids **27**, 044105 (2015).
10. J. I. Jimenez-Gonzalez and P. Brancher, Phys. Fluids **29**, 114101 (2017).
11. C. Canuto, M. Y. Hussaini, A. Quarteroni, and T. A. Zang, *Spectral Methods* (Springer, Berlin, 2007).

Translated by E. Chernokozhin